J. Fluid Mech. (2022), *vol*. 951, A30, doi:10.1017/jfm.2022.862

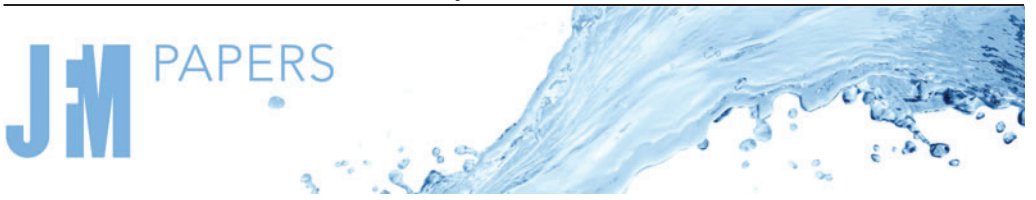

On axisymmetric dynamic spin coating with a single drop of ethanol

Yuming Pan[1], **Zhibei Wang**[1], **Xinyan Zhao**[1], **Weiwei Deng**[1,†] **and Huihui Xia**[1,†]

[1]Shenzhen Key Laboratory of Soft Mechanics & Smart Manufacturing, Department of Mechanics and Aerospace Engineering, Southern University of Science and Technology, Shenzhen 518055, PR China

(Received 9 November 2021; revised 1 October 2022; accepted 7 October 2022)

We carried out experimental and numerical investigations on the axisymmetric spreading evolution of dynamic spin coating with a single drop of ethanol. The results show that the dynamic spreading process consists of two stages: inertial spreading stage and centrifugal thinning stage. These two stages are connected by a transient state in between characterized by the minimum contact line moving velocity. The Weber number determines the spreading in the first stage, similar to the case of the impact of a drop on a static substrate. The rotational Bond number has a marginal effect on the inertia spreading and the radius at the transient state. In the centrifugal thinning stage, the rotational Bond number dominates the flow while the effect of the Weber number is negligible.

Key words: drops, rotating flows, coating

1. Introduction

Spin coating is a widespread film fabrication technique in research and industry (Soto-Montero, Soltanpoor & Morales-Masis 2020). It can conveniently and consistently produce a thin film with less than 1 % variation in thickness due to self-levelling of the liquid film (Frank *et al.* 1996). In spin coating, a small volume of coating material is dispensed onto a substrate, which is either already spinning (dynamic) or subsequently set to spin (static). Dynamic spin coating is often preferred because it requires less coating material than its static counterpart (Tyona 2013). Moreover, for coating of multiple layers, dynamic spin coating reduces the re-dissolving of the previous layer if the solvents are not strictly orthogonal (Yang, Kang & Kim 2017).

Many publications have helped to establish a profound understanding of the fluid dynamics of spin coating (Emslie, Bonner & Peck 1958; Schwartz & Roy 2004; Craster & Matar 2009; Primkulov *et al.* 2020), such as effects of fingering instabilities (Melo,

† Email addresses for correspondence: dengww@sustech.edu.cn, xiahh@sustech.edu.cn

Joanny & Fauve 1989; Sahoo, Orpe & Doshi 2018), non-Newtonian fluids (Lawrence & Zhou 1991), and solvent evaporation (Arscott 2020). However, the majority of prior works have focused on static dispensing, where the inertial effect of the landing drop on the spinning substrate is excluded. For impact of drops on static substrates, the Weber number $We = \rho u_0^2 R_0/\gamma$ (u_0, ρ and γ are respectively the impact velocity, density and surface tension of the liquid drop) describes the relative importance between the inertial and capillary effect and identifies deformation and spreading behaviours (Josserand & Thoroddsen 2016; Yonemoto & Kunugi 2017; Srivastava & Kondaraju 2020). In the dynamic spin-coating process, the Weber number also plays an important role, while its influence on the spreading process is still unclear. Moreover, the centrifugal effect for a spinning and spreading film of angular velocity ω should be considered. Because the characteristic pressure due to centrifugal acceleration is $\rho\omega^2 R^2$ (R is the film radius) and the capillary pressure is $\sim\gamma/h$ (h is the film thickness), one can define the rotational Bond number as the ratio between the two quantities (Melo *et al.* 1989; Wang & Chou 2001), $Bo_r = \rho\omega^2 r^2 h/\gamma = \rho\omega^2 V/\gamma$, with V being the drop volume. Here, Bo_r determines the critical radius R_c for the onset of fingering instability (Wang & Chou 2001), and the radius of the final film should be smaller than R_c to avoid fingering defects.

Another important challenge in applications of dynamic spin coating is to maintain the axisymmetry of the spreading droplet. Several experimental studies have been conducted of these non-axisymmetrically spreading cases (Li *et al.* 2011; Moghtadernejad *et al.* 2021). A bulk of waved liquid can be observed during spreading, which, however, is hazardous for film fabrication. In this paper, we design an experimental system to achieve axisymmetric dynamic spin coating. We aim to explore the influence of We and Bo_r during the axisymmetric spreading process. We carefully measure the film radius and film thickness as functions of time t with a high-speed camera and fluorescence photography. We consider the energy budget that offers insights into the spreading dynamics.

2. Methods

2.1. *Experimental methods*

As schematically depicted in figure 1, the liquid drop was dispensed from the tip of a vertically oriented nozzle by a syringe pump. We chose ethanol as its surface tension is similar to that of many common organic solvents used in spin coating of thin films, and the results will be more relevant. The inner and outer diameters of the nozzle were 0.4 and 0.7 mm, respectively. Depending on the wetting diameter at the nozzle (Tsai & Wang 2019), the drop radius R_0 was approximately a constant of 1.13 ± 0.04 mm in our experiments. Accordingly, the gravitational Bond number $Bo = \rho g R_0^2/\gamma \approx 0.45$. The substrate was a glass or silicon (covered by SiO_2) disk of 15 mm in diameter, which was attached to an electric motor. The disk radius was less than R_c ($\sim$8 mm) to avoid a fingering instability. Care was taken to ensure that the drop impacts at the centre of the rotating disk. The Weber number was changed by adjusting the release height of the drop (from 2 mm to 10 cm). Taking our targeted applications as an example, we are interested in the fabrication of organic photovoltaics using dynamic spin coating. One frequently used solvent is chloroform, whose surface tension is slightly larger than that of ethanol. The volume of the solution drop for spin coating is $\sim$8 µl and the drop is typically released at a height of a few centimetres (1–5 cm). The corresponding Weber number ranges from

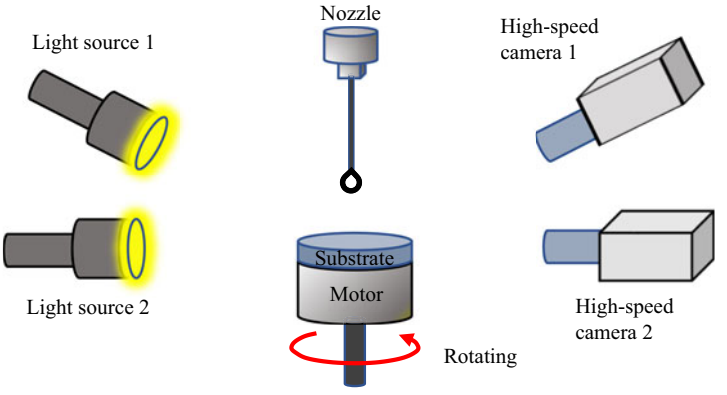

Figure 1. Schematic of experimental configuration of dynamic spin coating.

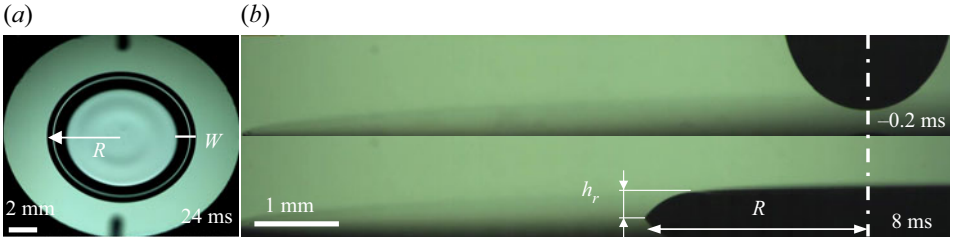

Figure 2. Snapshots of the dynamic spin-coating process obtained from (*a*) camera 1 and (*b*) camera 2, with an ethanol drop of 1.13 mm in radius and the rotating speed being 3000 rpm.

13 to 67, which is covered by the present work. The value of Bo_r spans from 10 to 65 via varying ω from 2000 to 5000 rpm.

The dynamic spin-coating process was recorded from oblique (with an angle of 45° to the horizontal plane) and side views using two synchronized high-speed cameras (i-SPEED 220, iX-cameras) and illuminated by two light-emitting diode light sources. The cameras were coupled with long-working-distance microscope lenses of adjustable magnifications. The typical frame rate was 4000 frames per second with an exposure time of 2 μs. The substrates were cleaned subsequently using lye, deionized water, acetone and isopropanol in an ultrasonic bath (each step for 15 min). Then the substrates were treated by oxygen plasma for 1 min. Each substrate was used only once for the dynamic spin-coating process before being retreated by plasma. The measured static contact angle for ethanol was below 10° for both the glass and SiO_2-covered silicon substrates.

Figure 2 shows snapshots of dynamic spin coating from the oblique and side views. A droplet of 6 μl was released at a height of ∼1 cm. As the droplet impacts the substrate and spreads radially, a thin inner film is formed in the middle with a capillary ridge around the perimeter. The spreading radius R, ridge width w and ridge height h_r were measured using the edge detection code with MATLAB. The impact velocity and Weber number can also be obtained from the side view ($u_0 = 0.53$ m s^{-1} and $We = 10$ in figure 2).

2.2. *Measurement of the film profile*

The measurement of the inner film thickness is rather challenging due to the fast spreading and view blockage by the ridge. To overcome this challenge, fluorescence photography

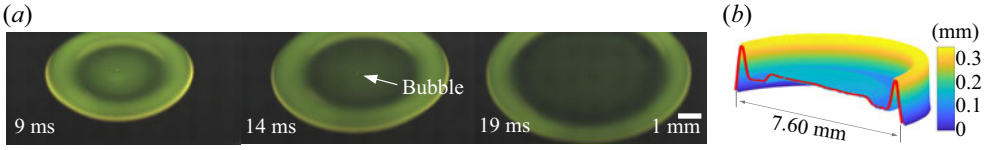

Figure 3. (*a*) Image sequences of the spreading drop based on the fluorescence intensity. (*b*) Film thickness profile based on the brightness of the fluorescence extracted from the image (at 9 ms).

(Alekseenko *et al.* 2012) was used. A fluorescent dye, rhodamine 6G (Rh6G), was doped in the liquid with a concentration of 0.3 mg ml^{-1}. The surface tension of this solution was measured as 22.0 mN m^{-1}, within 3 % of the value of pure ethanol. Excited by ultraviolet light, the Rh6G-doped drop emits a luminosity field $I(r)$, as shown in figure 3. The overall three-dimensional morphology of the spreading drop is reconstructed via image processing based on $I(r)$ with MATLAB (figure 3*b*). Because of its axisymmetry, the centreline profile of the film (denoted by the red curve) is extracted for further analysis (e.g. film volume calculations), instead of the whole three-dimensional surface. By this means, the distortion due to the tilted camera view on surface height reconstruction (especially the outer area of the ridge) is minimized. For thin films ($h < 1$ mm), $I(r)$ is linearly proportional to thickness by the Beer–Lambert law: $h = cI(r)$, with c being the proportionality constant (Alekseenko *et al.* 2012; Wang *et al.* 2022). An intuitive but sketchy method to determine c is comparing the ridge height h_r from the side-view shadowgraph and the corresponding value of $I(r)$ from fluorescence photography. Instead, we obtained c through calibration of the spreading drop volume, $V = \int_0^R 2\pi rh\,\mathrm{d}r = 2\pi c\Delta r \sum_i r_i I_i = cV'$, where c is indeed the averaged value along the radial direction, Δr is the sampling distance and V' is the integrated volume based on $I(r)$. As shown in figure 4(*a*), the time-averaged value of c is achieved through comparison with the original drop volume (6 µl), with an error of ± 1 µl, which is due to uncertainty associated with the measurements and limitation of image resolutions. Figure 4(*b*) further verifies the accuracy in thickness measurement by comparing h_r with the values obtained from the side-view shadowgraph method for both the mixture and pure ethanol cases.

2.3. *Numerical simulation method*

We perform numerical simulations of the dynamic spin-coating process using the open-source software Basilisk (Popinet *et al.* 2013–2021*b*), which is a finite-volume solver for the incompressible two-phase Navier–Stokes equations (Popinet 2009, 2015). It reconstructs the liquid–gas interface using the volume-of-fluid method based on a momentum-conserving scheme and incorporates the surface tension as a body force. The adaptive mesh refinement scheme allows one to save computing cost while resolving the multiscale problem involved in the spin-coating process. The characteristic length scale reduces from millimetres to micrometres while the drop impacts and continuously spreads on the solid substrate. Since the Coriolis force $2\omega u_\varphi \approx \rho r\omega^3 h^2/\mu$ (u_φ is the azimuthal velocity and μ is the liquid viscosity) is much smaller than the centrifugal force $r\omega^2$ (Emslie *et al.* 1958), it is neglected in this work. Other non-axisymmetric effects such as fingering instabilities and heterogeneous wetting on the substrate are also ignored. The evaporation effect on the spreading dynamics is also neglected, as the time scale for an evident volume loss due to evaporation is over two orders of magnitude (> seconds) larger than that of the spreading process (Gurrala *et al.* 2019).

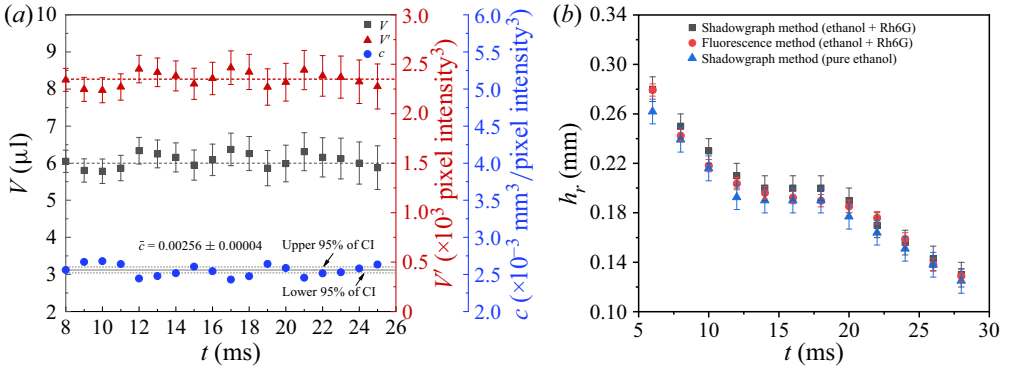

Figure 4. (*a*) Calibration of the fluorescence method by correlating the integrated volume with the original drop volume (6 μl); the mean value of the coefficient c is denoted by the horizontal solid line being the averaged value, and the dashed lines represent the lower and upper 95 % of confidence intervals (CI), respectively. (*b*) Evolution of the ridge height obtained from the fluorescence methodology and the side-view shadowgraph at $We = 10$ and $Bo_r = 23.4$. The error bars represent uncertainty associated with the measurements and limitation of image resolution.

A governing equation in the azimuthal (φ) direction is included (Yang *et al.* 2020), and the acceleration term due to spinning is incorporated in the governing equation to account for the centrifugal effect (Popinet *et al.* 2013–2021*a*). The size of the computational domain is 8×8 mm^2. The mesh is refined to level 11 so that the finest cell is 3.9 μm. The film thickness is about 20 μm when the drop is fully spread on the substrate, thus occupying five mesh cells. The bottom is no-slip boundary condition except the area in the vicinity of the liquid–solid interface (contact line) where the Robin boundary condition is applied. Because no-slip condition creates force singularity at the liquid–solid interface and phenomenologically traps a thin air film (<1 μm) between the drop and substrate that consistently impedes the contact of them, which is not observed in experiments. The Robin boundary condition is $\boldsymbol{u}_t = u_s - \lambda(\partial \boldsymbol{u}_t/\partial n)$, with $\boldsymbol{u}_t$ the tangential velocity at the boundary, u_s the substrate velocity, λ the slip length and n the inward normal to the surface. For simplicity, we set λ to be a constant of 1 μm, which is large enough to avoid such an unreal air film in our simulations. For the wetting condition, we employ an empirical dynamic contact angle model developed by Kistler (1993) based on Hoffman's law (Hoffman 1975). This dynamic angle θ is a function of the equilibrium contact angle θ_{eq} and the capillary number Ca regarding the contact line spreading velocity u_{cl}, written as

$$\theta = f_{Hoff}[Ca + f_{Hoff}^{-1}(\theta_{eq})], \tag{2.1}$$

with $Ca = \mu u_{cl}/\gamma$ and f_{Hoff}^{-1} being the inverse function of Hoffman's empirical function (Hoffman 1975), which is defined as

$$f_{Hoff}(x) = \arccos\left\{1 - 2\tanh\left[5.16\left(\frac{x}{1 + 1.31x^{0.99}}\right)^{0.706}\right]\right\}, \tag{2.2}$$

with $x = Ca + f_{Hoff}^{-1}(\theta_{eq})$. The contact line velocity u_{cl} is obtained by numerical differentiation of the wetting radius R, namely $u_{cl} = \mathrm{d}R/\mathrm{d}t$. Although Kistler's model was fitted from data where inertia can be ignored, the data still fall right on the model curve even when the Reynolds number is up to 250 as reported by Kistler. Kistler also reported the model fits well over the range $0.005 < Ca < 0.3$, which is satisfied in the present work.

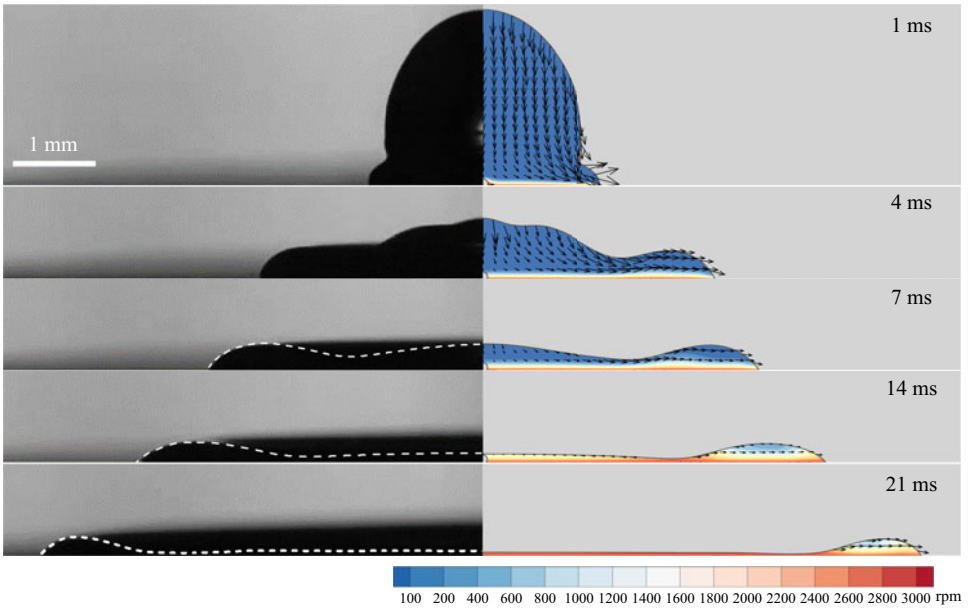

Figure 5. Comparison of a spreading ethanol drop shape obtained from experimental images and simulation results when $We = 10$, $Bo_r = 23.4$. The dashed curves show the liquid–air interfaces from the fluorescence method.

2.4. *Validation of the numerical simulation*

The numerical simulation is validated by comparing with experimental results. Figure 5 shows details of the spreading droplet obtained from side-view image sequences (left-hand panel), numerical simulations (right-hand panel) and the fluorescence method (dashed curves). For consistency, the initial drop profile in the simulation was extracted from that of the experiment, which was vertically prolate with the aspect ratio being 1.15. A qualitative comparison of the droplet profile demonstrates that this numerical method can capture the flow features of the spin-coating process, and also validates the accuracy of the thickness measurement using the fluorescence method. The velocity fields and contours of the rotation speed show that the drop deformation is dominated by the inertia of the free fall after impingement, similar to those of static substrate counterparts. An air bubble is trapped beneath the drop after impingement in simulations, as also found in figure 3. The bubble remains stationary in the drop centre and then bursts when the spreading velocity reaches the minimum (at $\sim$15 ms), after which spreading is dominated by the centrifugal force (details are discussed in the next section). It is noted that the drop always oscillates after pinching off from the nozzle as observed in experiments. The aspect ratio (vertical width a to horizontal width b) of the drop in our experiments is within (0.85, 1.2). Our simulations comparing droplets of different aspect ratios demonstrate that the oscillation/deformation of the drop only contributes slightly at the early stage after impact and negligibly on the transition of the stages and centrifugal thinning stage, as shown in figure 6. Therefore, for simplicity we initialize the drop as a sphere in further simulations.

The quantitative comparison (figure 7) of the corresponding dynamic contact angle and contact line moving velocity during spreading also demonstrates the good consistency between the experiment and simulation. The dynamic contact angle is positively correlated with the spreading velocity, as given by (2.1). Angle θ decreases rapidly after impacting

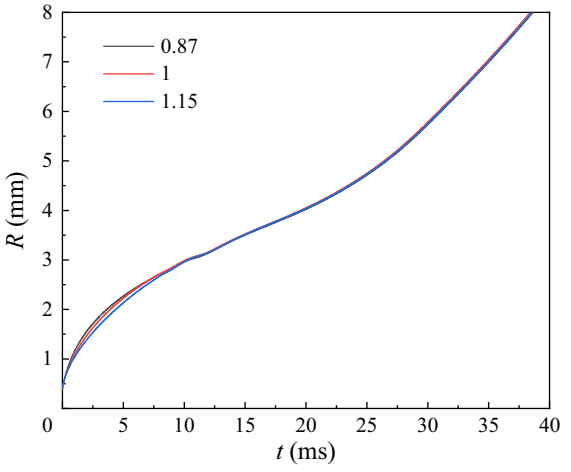

Figure 6. Comparison of the spreading radius at three vertical aspect ratios, 0.87, 1 (sphere) and 1.15, when $Bo_r = 23.4$ and $We = 10$.

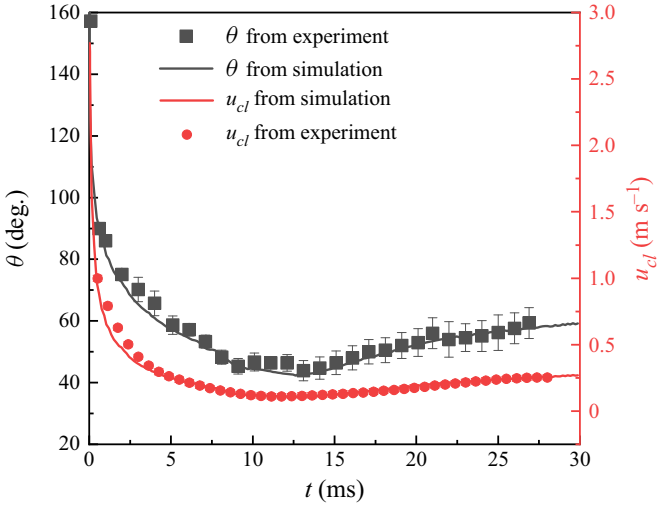

Figure 7. Comparison of the dynamic contact angle and spreading velocity under the conditions corresponding to figure 5.

and reaches a minimum value of 42° when $u_{cl} \approx 0.1$ m s^{-1}, after which θ gradually increases to ~60° when reaching the disk edge.

3. Results and discussion

3.1. *Evolution of the spreading radius throughout the dynamic spin-coating process*

The dynamic spin-coating process can be divided into two stages: (I) inertial spreading stage and (II) centrifugal thinning stage. The first stage begins immediately after drop impingement (figure 5): the bottom of the drop is sheared by the rotating substrate, while the upper part still descends due to inertia of free fall. In this stage, the spreading is mainly affected by the factors similar to classical drop impingement onto a stationary substrate,

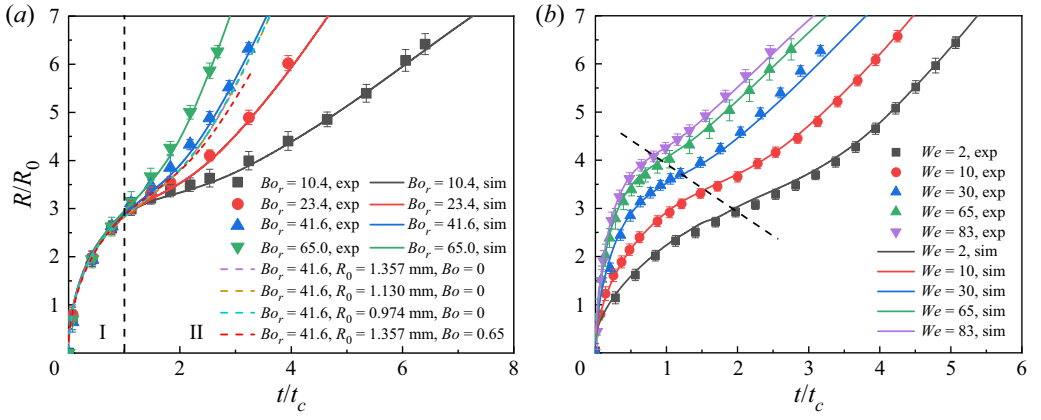

Figure 8. Time evolution of the drop spreading radius at (*a*) various Bo_r numbers when $We = 10$ and (*b*) various *We* numbers when $Bo_r = 23.4$. The error bars represent uncertainty associated with the measurements of the spreading radius. Here, $Bo = 0.45$ and $R_0 = 1.13$ mm if not specified.

such as the Weber number, viscosity and contact angle on the substrate. The rotational motion of the substrate is transferred upwards due to viscous shearing. Since the liquid film is continuously accelerated in the azimuthal direction, it enters the centrifugal thinning stage after a certain period.

Figure 8 shows the time evolution of the spreading film radius obtained in experiments and those from simulations at various *We* and Bo_r. The time is normalized by the capillary time t_c and the spreading radius is normalized by R_0. In general, the spreading time decreases with increased *We* and Bo_r. At the early stage after drop impingement, $R(t)$ exhibits a steep slope, demonstrated as a function of the Weber number. The rotational Bond number has marginal effects on the spreading radius evolution during this stage, which is also confirmed by the velocity fields in figure 5. The spreading radius here follows a square-root dependence, $R \sim t^{1/2}$, even when the gravitational Bond number varies. This observation is similar to that for drops impacting on stationary substrates (Josserand & Thoroddsen 2016). In that case, a maximum wetting radius exists before the drop retracts (Yonemoto & Kunugi 2017). Correspondingly, a transient spreading radius (marked by the dashed lines) exists here when the spreading velocity reaches the minimum due to viscous dissipation and interaction with the substrate. The time required for the film spreading to the transient radius (R_t) is positively correlated with the Weber number, while independent of Bo_r. The transition from stage I to II is demarcated by the black dashed line. In stage II, the centrifugal force becomes increasingly important and is responsible for further expanding of the film. It is also found that *Bo* plays a role in the spreading velocity but not the general trend. For a small *Bo*, i.e. a drop smaller than the capillary length scale, this role is minor.

3.2. *Evolution of the spreading radius and film thickness in the centrifugal thinning regime*

In the spreading regime where centrifugation dominates, the spreading radius R and film thickness h are functions of ω and fluid properties. Following Melo's principle (Melo *et al.* 1989), R and t are normalized by $R' = V^{1/3}Bo_r$ and $t' = V^{1/3}\mu/\gamma$, respectively. It should be noted that R' and t' are different from the original expressions in the work of Melo *et al.*, while still satisfying the Buckingham π theorem, $R/R' = f(t/t', Bo_r)$. Figure 9

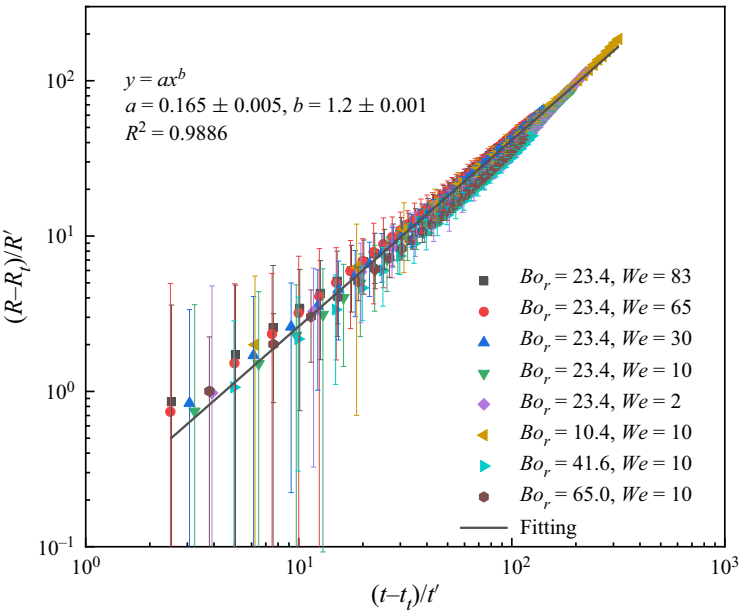

Figure 9. Normalized spreading radius R/R' as a function of the dimensionless time t/t'.

replots the extracted data in the centrifugal thinning regime at different We and Bo_r from figure 8. A power-law fitting with the scaling exponent being 1.2 ± 0.001 is obtained. This correlation deviates significantly from asymptotic scaling (Fraysse & Homsy 1994; Oron, Davis & Bankoff 1997), $R \sim t^{1/4}$, whose second derivative is negative rather than positive as observed in our experiments and simulations. This is because the previous asymptotic scaling was derived from the lubrication theory based on the assumption of a flat film. Indeed, a capillary ridge is formed and accounts for a large portion of the spreading film as seen in figures 2 and 3. Considering the spreading is dominated by centrifugation, the scaling of $R \sim t^{1.2}$ is reasonable and helps to explain the nearly constant contact line moving velocity in the later stage of drop spreading when the viscous effect becomes more important.

Figure 10 depicts the normalized inner film thickness versus the dimensionless time. The thinning of the film asymptotically follows the classical power law, i.e. $h \sim t^{-1/2}$, where the viscous shear force balances the centrifugal force, and surface tension is neglected (Oron *et al.* 1997). A possible explanation is that the flow in the inner film satisfies the lubrication approximation in the developed stage of the centrifugal thinning regime. For instance, at $t = 21$ ms in figure 5, the inner film becomes very thin and flat, and the profile of the radial velocity in the vertical direction is parabolic. We noticed that in the prior work by Middleman (1987), the film-thinning scaling exponent is -1, where the effect of the air shear stress is considered. Following Middleman's definitions and derivation, a dimensionless time τ and a dimensionless film thickness H are given as $\tau = (2\rho\omega^2 h_0^2/3\mu)t$ and $H = h(t)/h_0$, where h_0 is the initial uniform thickness of the film. The correlation between the dimensionless film thickness H and time τ is expressed as

$$\tau = \beta\left(\frac{1}{H} - 1\right) - \beta^2 \ln\left(\frac{1+\beta H}{H(1+\beta)}\right), \tag{3.1}$$

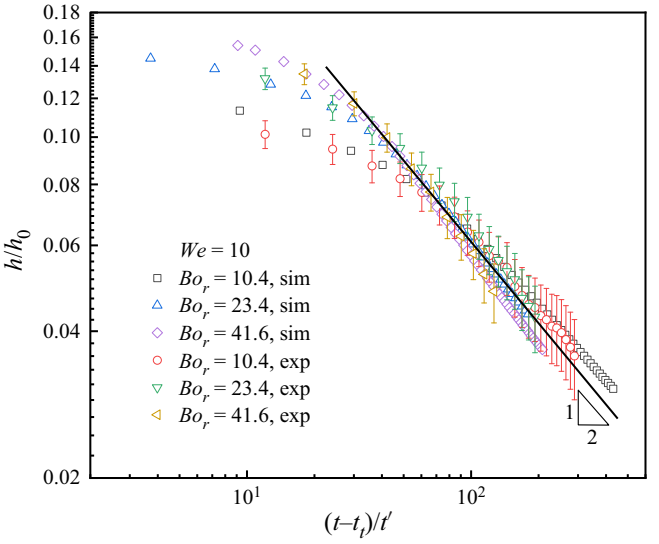

Figure 10. Normalized inner film thickness h/h_0 plotted against the dimensionless time t/t_0 at various Bo_r numbers when $We = 10$. The triangle represents the slope of the black line. The error bars represent uncertainty associated with the measurements of the film thickness.

where the dimensionless parameter $\beta = 4h_0\omega^{1/2}\rho/(3\rho_{air}\nu_{air}^{1/2})$, with ρ_{air} and ν_{air} being the density and kinetic viscosity of air. In most applications, β is large (of the order of 10^2 to 10^3 in the current work). In Middleman's work, the second term is considered to approach zero, yielding $\tau \sim H^{-1}$. However, we find that the second term cannot be neglected. With the logarithm term in (3.1) being expanded into a Taylor series to the second order, it can be rewritten as

$$\tau \approx \frac{\beta}{\beta+1}\left(\frac{1}{H}-1\right)+\frac{\beta^2}{(1+\beta)^2}\frac{(1-H)^2}{2H^2}. \tag{3.2}$$

Therefore, even considering the air-shear effect, the thinning of the inner film still satisfies $H \sim \tau^{-1/2}$ for a large β, rather than $H \sim \tau^{-1}$.

3.3. *Energy budget analysis*

Analysis of the energy budget is an approach commonly used to study energy partition and transformation (Lee *et al.* 2016; Ye, Yang & Fu 2016; Huang & Chen 2018; He, Xia & Zhang 2019; Sanjay, Lohse & Jalaal 2021). Film spreading on a spinning substrate is governed by the balance between kinetic energy (E_k), surface energy (E_s), gravitational potential energy (E_g), viscous dissipated energy (E_Φ) and shear work (E_τ) imposed on the drop by the rotating substrate. We trace the evolution of the energy sources to give an insight into the dynamics during the spin-coating process by showing how it experiences the transition of spreading regimes. The energy equation for the axisymmetric dynamic spin-coating process is

$$E_{k1}+E_{s1}+E_{g1} = E_{k2}+E_{s2}+E_{g2}+E_\Phi-E_\tau, \tag{3.3}$$

where subscripts 1 and 2 denote the time at drop impact and an arbitrary moment during spreading, respectively. Term E_g is neglected in the energy budget analysis during

spreading, as $Bo < 1$ and the initial gravity potential at the release height is almost converted into kinetic energy at impact. Each term is written as follows:

$$E_k = E_{kr} + E_{k\varphi} + E_{kz} = \frac{1}{2}\int_V |\boldsymbol{u}|^2 \,\mathrm{d}V, \tag{3.4}$$

$$E_s = \gamma A_{lg} + E_{ls}, \tag{3.5}$$

$$E_\Phi = \int_{t_1}^{t_2}\int_V \Phi \,\mathrm{d}V \,\mathrm{d}t, \tag{3.6}$$

$$E_\tau = \int_{t_1}^{t_2} \boldsymbol{F}_{\tau(r,\varphi)} \cdot \boldsymbol{u}_{(r,\varphi)} \,\mathrm{d}t, \tag{3.7}$$

with E_{kr}, $E_{k\varphi}$ and E_{kz} being the kinetic energy in the radial (r), azimuthal (φ) and axial (z) directions, $\boldsymbol{u} = (u_r, u_\varphi, u_z)$ the velocity vector, A_{lg} the liquid–air interface area, Φ the viscous dissipation rate and $\boldsymbol{F}_{\tau(r,\varphi)} \approx \mu \int_{A_{ls}} (\partial u_r/\partial z, \partial u_\varphi/\partial z)|_{z=0} r \,\mathrm{d}A_{ls}$ the shear force vector at the liquid–solid interface (A_{ls}) at the wall $z = 0$. Parameter E_{ls} is the surface energy at the liquid–solid interface and contact line and obtained from (3.3). The dissipation due to capillary hysteresis is not considered, as this effect occurs only when the substrate is swept by both an advancing and a receding contact line (Yue 2020).

Figure 11 shows representative examples of the energy budget evolution obtained from simulations. The energy terms are normalized by the total energy $E_{total} = E_k + E_s + E_\Phi$, which increases continuously due to the input energy E_τ. Initially, upon drop impact ($t = 0$ ms), the drop's energy is stored as surface energy E_s and kinetic energy E_{kz} (∼60 % of E_{total} for $We = 10$, and ∼90 % for $We = 65$). After impingement, E_{kz} is rapidly converted to E_s, E_{kr}, and partially consumed by viscous dissipation E_Φ, as the drop spreads in the radial direction. The larger the Weber number, the higher the portion of E_{kr} that is reached. For $We = 65$, E_{kr} reaches ∼40 % of the total energy after growth for a short duration (∼1 ms) and then declines to a low level (<5 %) at the transient state. Meanwhile, the surface energy increases rapidly and eventually dominates during the transient state. The higher the value of We, the higher the percentage the surface energy reaches (>70 % for $We = 65$), as the drop spreads faster and further. The proportion of the viscous dissipation in the total energy budget is positively correlated with We and Bo_r due to stronger viscous shear from the rotating disk. This is consistent with the finding for a drop impacting on a stationary substrate in that viscous dissipation increases with impact velocity (Lee *et al.* 2016).

After the transient state, $E_{k\varphi}$ increases monotonically, and the film spreading enters the centrifugal thinning stage. The bulk liquid is continuously accelerated in the azimuthal direction due to shearing from the substrate. Consequently, the velocity in the radial direction is increased. However, due to the countering viscous stress from the substrate and thinning of the film, E_{kr} accounts for less than 5 % of the total energy. During the centrifugal thinning stage, E_s continues rising, approximately as $E_s \sim R^2$. However, the percentage of E_s to E_{total} decreases, as $E_{k\varphi}$ increases more rapidly due to the azimuthal acceleration of the bulk liquid and increasing spreading radius (also $\sim R^2$).

3.4. *Radius at transition from inertia to centrifugal regime*

Analogous to the case of drop impingement on a static substrate (Srivastava & Kondaraju 2020), there exists a transient state at R_t for the dynamic spin-coating process when the radial spreading velocity $u_{cl} = \mathrm{d}R(t)/\mathrm{d}t$ reaches the minimum. Figure 12 shows the

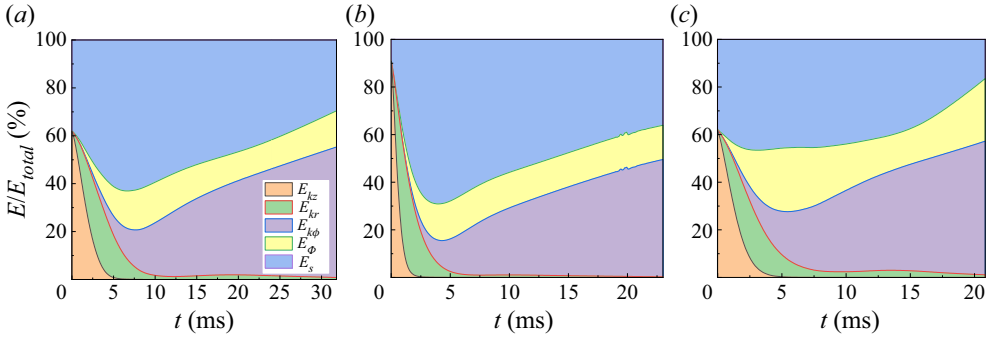

Figure 11. Energy budget for the dynamic spin-coating process with (*a*) $We = 10$, $Bo_r = 23.4$, (*b*) $We = 65$, $Bo_r = 23.4$ and (*c*) $We = 10$, $Bo_r = 65$.

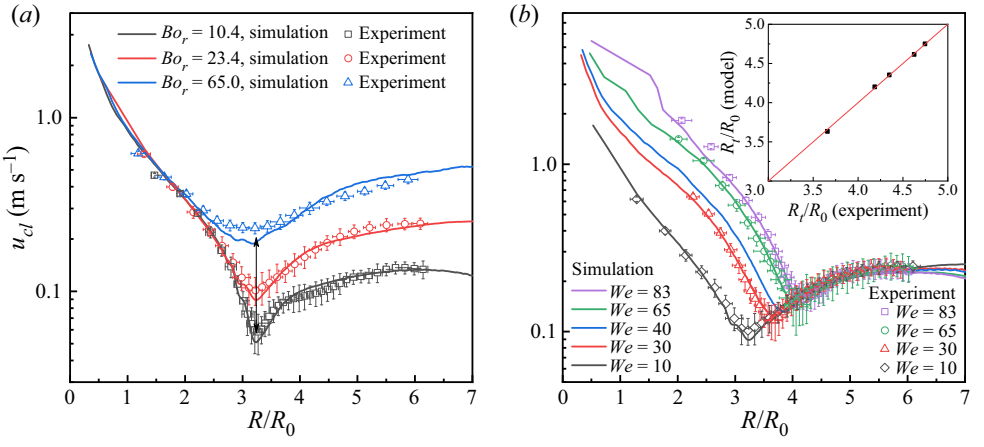

Figure 12. Radial spreading velocity (contact line moving velocity) plotted against the dimensionless spreading radius at different (*a*) Bo_r when $We = 10$ and (*b*) We when $Bo_r = 23.4$. The inset shows a comparison of the dimensionless transient radius of (3.8) with the simulated data. The error bars represent uncertainty associated with the measurements of the spreading radius.

spreading velocity against the dimensionless spreading radius by changing either Bo_r or We. The results indicate that Bo_r has marginal effects on R_t. For larger Weber numbers, R_t increases. During the initial impact stage, the relationship between R_t and We is similar to that of drops impacting on stationary substrates.

Many researchers have developed models for such R versus We based on energy conservation without considering the rotational shearing work from the substrate (Clanet *et al.* 2004; Attané, Girard & Morin 2007; Roisman 2009; Josserand & Thoroddsen 2016; Lee *et al.* 2016; Yonemoto & Kunugi 2017; Srivastava & Kondaraju 2020). If we assume an infinitely large Weber number, the effect of the rim can be neglected, and the film thickness is approximately uniform. Accordingly, the magnitude of R_t is similar to the scaling relationship $R_t \sim Re^{1/5} \sim We^{1/10}$, as obtained for the case where a drop impacts a static substrate (Clanet *et al.* 2004), where $Re = 2\rho u_0 R_0/\mu$ is the Reynolds number. However, the Weber number is finite and as found in figure 13 the volume of the rim cannot be ignored. In previous work (Roisman 2009), a characteristic length $L_R \sim Re^{2/5} We^{-1/2}$ is incorporated to account for the influence of the rim motion, which

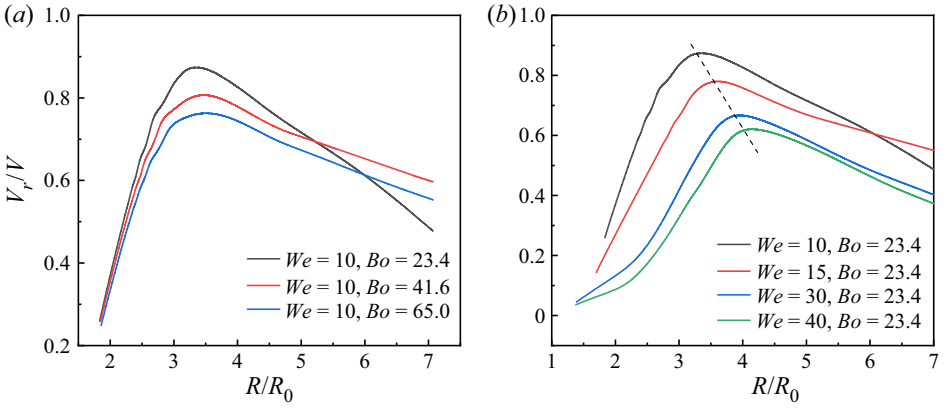

Figure 13. Evolution of the ridge volume ratio at (*a*) various Bo_r when $We = 10$ and (*b*) various We when $Bo_r = 23.4$.

should be inversely correlated with R_t. As shown in the inset of figure 12(*b*), we fit the obtained data using the linear combination of the two terms following Roisman's method, leading to a semiempirical relation:

$$R/R_0 \approx 1.03\, Re^{1/5} - 0.08\, Re^{2/5}\, We^{-1/2}. \tag{3.8}$$

It is found that the coefficient of the second term on the right-hand side of (3.8) is much smaller than that of the first term. This indicates that the role of the rim is less important during spreading, for $886 < Re < 2553$ and $10 < We < 83$ in this work.

3.5. *Evolution of the ridge volume*

Figure 13 shows the evolution of the ridge volume V_r (normalized by the drop volume V) as a function of the spreading radius at various Bo_r and We. Here, we consider that the ridge and the inner film are separated at the thinnest area based on the interface profile. The volume is rapidly accumulated in the ridge area in the inertia-dominated regime. Because the contact line moving velocity u_{cl} decreases after drop impingement (see figure 12), the top of the drop continues to descend. The liquid in the centre is continuously fed into the ridge. The ridge volume peaks at the transient state, as marked by the dashed line. This observation is similar to the evolution of u_{cl}, that is, where V_r peaks is independent of Bo_r and increases with We. Besides, when either Bo_r or We decreases, the spreading is slower, and more liquid is confined in the ridge. As a result, the maximum ridge volume at the transient state decreases with increased Bo_r and We, where it is up to $\sim$90 % of the total volume for $We = 10$ and $Bo_r = 23.4$. After the transient state, the ridge volume declines approximately linearly against the spreading radius.

4. Conclusions

The process of dynamic spin coating has been experimentally and numerically investigated. The approach based on the fluorescence method has shown good accuracy in the measuring of the film-thickness profile via cross-validation with the two-dimensional numerical model. The spreading process is analysed in the range of $1 < We < 83$, $10 < Bo_r < 65$. The results show that We plays a major role in drop spreading in the early

times after drop impingement, where inertia dominates. The spreading radius in this stage follows a power law, $R \sim t^{1/2}$, and the dependence of the spreading radius on *We* is close to $R \sim We^{1/10}$ at the transient state. The role of the rotational Bond number becomes important in the latter stage, where centrifugation dominates. The time evolution of the spreading radius is obtained as $R \sim t^{1.2}$, and the film thickness is $h \sim t^{-1/2}$.

Acknowledgements. Simulations were performed on the Taiyi high-performance supercomputer cluster, supported by the Center for Computational Science and Engineering at SUSTech.

Funding. This work was financially supported by the National Natural Science Foundation of China (grant numbers 11932009, 61975073, 11872199); the Science, Technology and Innovation Commission of Shenzhen Municipality (grant number ZDSYS20210623092005017); and GuangDong Basic and Applied Basic Research Foundation (grant number 2020A1515110268).

Declaration of interests. The authors report no conflict of interest.

Author ORCIDs.
Weiwei Deng https://orcid.org/0000-0002-8331-9249;
Huihui Xia https://orcid.org/0000-0002-8587-8407.

References

Alekseenko, S., Cherdantsev, A., Cherdantsev, M., Isaenkov, S., Kharlamov, S. & Markovich, D. 2012 Application of a high-speed laser-induced fluorescence technique for studying the three-dimensional structure of annular gas–liquid flow. *Exp. Fluids* **53**, 77–89.

Arscott, S. 2020 The limits of edge bead planarization and surface levelling in spin-coated liquid films. *J. Micromech. Microengng* **30**, 025003.

Attané, P., Girard, F. & Morin, V. 2007 An energy balance approach of the dynamics of drop impact on a solid surface. *Phys. Fluids* **19**, 012101.

Clanet, C., Béguin, C., Richard, D. & Quéré, D. 2004 Maximal deformation of an impacting drop. *J. Fluid Mech.* **517**, 199–208.

Craster, R.V. & Matar, O.K. 2009 Dynamics and stability of thin liquid films. *Rev. Mod. Phys.* **81**, 1131–1198.

Emslie, A.G., Bonner, F.T. & Peck, L.G. 1958 Flow of a viscous liquid on a rotating disk. *J. Appl. Phys.* **29**, 858–862.

Frank, C.W., Rao, V., Despotopoulou, M.M., Pease, R.F.W., Hinsberg, W.D., Miller, R.D. & Rabolt, J.F. 1996 Structure in thin and ultrathin spin-cast polymer films. *Science* **273**, 912–915.

Fraysse, N. & Homsy, G.M. 1994 An experimental study of rivulet instabilities in centrifugal spin coating of viscous Newtonian and non-Newtonian fluids. *Phys. Fluids* **6**, 1491–1504.

Gurrala, P., Katre, P., Balusamy, S., Banerjee, S. & Sahu, K.C. 2019 Evaporation of ethanol-water sessile droplet of different compositions at an elevated substrate temperature. *Intl J. Heat Mass Transfer* **145**, 118770.

He, C., Xia, X. & Zhang, P. 2019 Non-monotonic viscous dissipation of bouncing droplets undergoing off-center collision. *Phys. Fluids* **31**, 052004.

Hoffman, R.L. 1975 A study of the advancing interface. I. Interface shape in liquid–gas systems. *J. Colloid Interface Sci.* **50**, 228–241.

Huang, H.-M. & Chen, X.-P. 2018 Energetic analysis of drop's maximum spreading on solid surface with low impact speed. *Phys. Fluids* **30**, 022106.

Josserand, C. & Thoroddsen, S.T. 2016 Drop impact on a solid surface. *Annu. Rev. Fluid Mech.* **48**, 365–391.

Kistler, S.F. 1993 Hydrodynamics of wetting. In *Wettability* (ed. J.C. Berg), pp. 311–429. Marcel Dekker.

Lawrence, C.J. & Zhou, W. 1991 Spin coating of non-Newtonian fluids. *J. Non-Newtonian Fluid Mech.* **39**, 137–187.

Lee, J.B., Derome, D., Guyer, R. & Carmeliet, J. 2016 Modeling the maximum spreading of liquid droplets impacting wetting and nonwetting surfaces. *Langmuir* **32**, 1299–1308.

Li, J.Y., Yuan, X.F., Han, Q. & Xi, G. 2011 Impact patterns and temporal evolutions of water drops impinging on a rotating disc. *Proc. Inst. Mech. Engrs* C*: J. Mech. Engng Sci.* **226**, 956–967.

MELO, F., JOANNY, J.F. & FAUVE, S. 1989 Fingering instability of spinning drops. *Phys. Rev. Lett.* **63**, 1958–1961.

MIDDLEMAN, S. 1987 The effect of induced air-flow on the spin coating of viscous liquids. *J. Appl. Phys.* **62**, 2530–2532.

MOGHTADERNEJAD, S., JADIDI, M., JOHNSON, Z., STOLPE, T. & HANSON, J. 2021 Droplet impact dynamics on an aluminum spinning disk. *Phys. Fluids* **33**, 072103.

ORON, A., DAVIS, S.H. & BANKOFF, S.G. 1997 Long-scale evolution of thin liquid films. *Rev. Mod. Phys.* **69**, 931–980.

POPINET, S. 2009 An accurate adaptive solver for surface-tension-driven interfacial flows. *J. Comput. Phys.* **228**, 5838–5866.

POPINET, S. 2015 A quadtree-adaptive multigrid solver for the Serre–Green–Naghdi equations. *J. Comput. Phys.* **302**, 336–358.

POPINET, S., *et al.* 2013–2021*a* Azimuthal Velocity for Axisymmetric Flows. Available at: http://www.basilisk.fr/src/navier-stokes/swirl.h [Accessed 8 October 2021].

POPINET, S., *et al.* 2013–2021*b* Basilisk. Available at: http://basilisk.fr [Accessed 8 October 2021].

PRIMKULOV, B.K., PAHLAVAN, A.A., BOUROUIBA, L., BUSH, J.W.M. & JUANES, R. 2020 Spin coating of capillary tubes. *J. Fluid Mech.* **886**, A30.

ROISMAN, I.V. 2009 Inertia dominated drop collisions. II. An analytical solution of the Navier–Stokes equations for a spreading viscous film. *Phys. Fluids* **21**, 052104.

SAHOO, S., ORPE, A.V. & DOSHI, P. 2018 Spreading dynamics of superposed liquid drops on a spinning disk. *Phys. Fluids* **30**, 012110.

SANJAY, V., LOHSE, D. & JALAAL, M. 2021 Bursting bubble in a viscoplastic medium. *J. Fluid Mech.* **922**, A2.

SCHWARTZ, L.W. & ROY, R.V. 2004 Theoretical and numerical results for spin coating of viscous liquids. *Phys. Fluids* **16**, 569–584.

SOTO-MONTERO, T., SOLTANPOOR, W. & MORALES-MASIS, M. 2020 Pressing challenges of halide perovskite thin film growth. *APL Mater.* **8**, 110903.

SRIVASTAVA, T. & KONDARAJU, S. 2020 Analytical model for predicting maximum spread of droplet impinging on solid surfaces. *Phys. Fluids* **32**, 092103.

TSAI, P.-H. & WANG, A.-B. 2019 Classification and prediction of dripping drop size for a wide range of nozzles by wetting diameter. *Langmuir* **35**, 4763–4775.

TYONA, M. 2013 A theoritical study on spin coating technique. *Adv. Mater. Res.* **2**, 195.

WANG, M.-W. & CHOU, F.-C. 2001 Fingering instability and maximum radius at high rotational Bond number. *J. Electrochem. Soc.* **148**, G283.

WANG, Z., ZHANG, C., XIA, H., XIE, Q. & DENG, W. 2022 Axisymmetric thin film flow on a flat disk foil subject to intense radial electric fields. *Phys. Fluids* **34**, 012109.

YANG, F., KANG, D.-W. & KIM, Y.-S. 2017 Improved interface of ZnO/$CH_3NH_3PbI_3$ by a dynamic spin-coating process for efficient perovskite solar cells. *RSC Adv.* **7**, 19030–19038.

YANG, W., DELBENDE, I., FRAIGNEAU, Y. & MARTIN WITKOWSKI, L. 2020 Large axisymmetric surface deformation and dewetting in the flow above a rotating disk in a cylindrical tank: spin-up and permanent regimes. *Phys. Rev. Fluids* **5**, 044801.

YE, H.Y., YANG, L.J. & FU, Q.F. 2016 Instability of viscoelastic compound jets. *Phys. Fluids* **28**, 043101.

YUE, P. 2020 Thermodynamically consistent phase-field modelling of contact angle hysteresis. *J. Fluid Mech.* **899**, A15.

YONEMOTO, Y. & KUNUGI, T. 2017 Analytical consideration of liquid droplet impingement on solid surfaces. *Sci. Rep.* **7**, 2362.